Electrochemical studies of steel rebar corrosion in clay: Application to a raw earth concrete

Joanna Eid, Hisasi Takenouti, Bachir Ait Saadi, Said Taibi

HAL Id: hal-02868061
https://hal.science/hal-02868061

Submitted on 9 Nov 2020

Electrochemical study of steel rebar corrosion in clay: Application to a raw earth concrete.

Joanna Eid[1,2]*, **Hisasi Takenouti[3], Bachir Ait Saadi[4], Said Taibi[1]**

[1] *Laboratoire Ondes et Milieux Complexes, UMR 6294, CNRS - Normandie Université, Université Le Havre Normandie, 53 rue Prony, 76600 Le Havre, France, said.taibi@univ-lehavre.fr*

[2] *Civil Engineering Department, Holy Spirit University of Kaslik (USEK), Jounieh, Lebanon, joannaeid@usek.edu.lb*

[3] *Laboratoire Interfaces et Systèmes Electrochimiques, UMR 8235, CNRS - Sorbonne Université, 4 place Jussieu, 75252 Paris CEDEX 05, France, hisasi.takenouti@upmc.fr*

[4] *Laboratoire de microscopie électronique et des sciences des matériaux, Université Sciences & Technologie d'Oran, BP 1505, El Ménaouer, Oran, Algeria, bac.aitsaadi@gmail.com*

* Corresponding author. E-mail: joannaeid@hotmail.com; Phone: +33 6 4862 9147; +961 9 600 931

Abstract

Reinforcement feasibility of a new ecological earth concrete was examined. Steel rebar corrosion, when in contact with three different types of clayey soil, was investigated using electrochemical methods, potentiodynamic voltammetry and impedance spectroscopy (EIS). Results have shown that the voltammetry method overestimates the corrosion rate while EIS supplies the most reliable results. Corrosion rate decreased and a steady state was reached after four months of contact. The type of clay does not have a significant influence on the corrosion rate of the steel rebar, and the average value of 3 $\mu m/year$ was considered acceptable for the lifetime of the structure.

Keywords: raw earth concrete, eco-materials, clay-steel interaction, electrochemical analyses, polarization resistance, EIS.

1. Introduction

Nowadays, ecological issues are important in the field of construction and civil engineering. Standard concrete requires, for its production, huge grey energy consumption. In addition, it needs natural aggregates, as sand and gravel, having significant impacts on the nature [1], like the destruction of beaches and mountains [2].

In order to reduce the environmental impact of standard concrete, the use of energy-efficient materials is necessary [3]. Therefore, many researchers tend to study the behaviour of eco-geo-materials, as new construction resources, such as dredged sediment, recycled aggregates, or raw earth [4] [5]. One of the alternatives is using natural soils (raw earth) as a basic material.

A new earth concrete was developed and patented in Normandy, France [6] [7] [8]. It is composed of 87 % of raw earth treated with 9% of cement and/or 3% of lime. It can also be strengthened with recycled concrete aggregates RCA [9] to improve its mechanical properties while remaining ecological. This earth concrete presents a satisfactory mechanical behaviour when structural elements are acting in compression, e.g. bearing walls. However, as in the case of standard concrete, when structural elements are working in bending or tension, e.g. beams, the concrete presents a low tensile strength which requires the use of steel reinforcements. Likewise, this low tensile strength affects the shrinkage behaviour of the earth concrete [10]. Using ecological reinforcements such as bamboo, liana, or vegetable fibres can be possible in the future with advanced studies [11] [12]. Thus, with the new earth concrete, steel reinforcement is still necessary to construct buildings, with structural elements acting in tension.

In the standard concrete, the environment is alkaline (pH value as high as 12.5). This environment promotes the formation of a protective film on the steel surface, which reduces

the corrosion rate [13]. However, due to the porosity of concrete, carbonation [14] and ingress of chloride ions [15] may occur, which will decrease the pH value and stimulate the corrosion process. In earth concrete, the environment is also alkaline, when it is treated with binders (cement and lime), but it is also composed of natural clayey soil that is not inert, like the case of sand and gravel present in standard concrete. So, to study the corrosion of steel in earth concrete, the interaction between the natural clayey soil and the steel should be considered.

Natural soil is a highly non-homogeneous environment, composed of different minerals and chemical compounds. Many soil parameters influence the corrosion of the steel [16] which are the particle size [17] [18], pH [19], moisture content [20] [21], concentration of dissolved oxygen [21] [22], nature of salt ions, and organic content [23]. According to the soil's particle size distribution, its resistivity varies and affects significantly the corrosion of the steel in soil [23]. Among minerals, clays are the most reactive with their environment with the presence of water; they increase soil's conductivity [16]. So, understanding their interaction with the steel is highly important, especially when the soil is used to construct buildings.

Studies reported in the literature discuss mostly bentonite-iron interaction. El-Shamy et al. [20] showed that the corrosion rate of pipelines in contact with bentonite is proportionally related to water content, as large as the moisture content is below 40%. Kaufhold et al. [24] showed that Na-bentonites are slightly less corrosive than Ca-bentonites, and that highly charged smectites are less corrosive than low charged ones. They also found out a formation of a 1:1 Fe-silicate mineral. Earlier, Ishidera et al. [25], also found out that the smectite clay was destabilized to form a 1:1 phyllosilicate. Schlegel et al. [26] showed a transformation in clay layers and a decrease in the corrosion rate with time. In iron-rich clay, Yan et al. [27] showed that the presence of Fe oxides in clay increases the reaction rate for both anodic and cathodic processes of pipeline steel.

Different techniques are proposed to evaluate the corrosion process and to measure the corrosion rate. Among all, electrochemical techniques are the most used. In different studies, the electrochemical impedance spectra showed two relaxation time constants with capacitive behaviour [16] [27].

The literature review shows that many studies dealt with the interaction between soil and carbon steel in the fields of archaeology [28] [29], pipelines [30], and radioactive waste management [24] [31]. These environments (high temperature, anaerobic, compacted soil, etc…) are very different from those of construction. In this field, only a few studies were devoted to earth walls and backfill reinforcement [32]. As far as we know, no study dealt with the corrosion of steel rebars in contact with earth concrete.

The aim of this paper is to investigate the corrosion rate of steel rebars embedded in raw earth. Results will validate the feasibility of reinforced earth concrete.

2. Methods

When a steel rebar is in contact with soil, the corrosion process takes place [33] [34] [35]. In this study, the interaction between a carbon steel rebar and three types of clayey soil, kaolinite, montmorillonite and natural silt, was investigated using two electrochemical methods to estimate the corrosion rate [36] [37].

2.1. Principles of electrochemical methods

A classical three electrodes cell constituted of a working (WE), a reference (RE) and a counter electrode (CE) was used. Electrodes were in contact with the clay which is a corrosive environment that constitutes the electrolyte. These electrodes were connected to a potentiostat which is both a control and a measuring device. It maintains the potential of the WE constant with respect to the RE by adjusting the current at the CE.

Generally, to study an electrochemical corrosion system, three main measurements can be done, open circuit potential (OCP, or E_{oc}), potentiodynamic polarizations (also called potentiodynamic voltammetry) that estimate the corrosion current density (I_c) and Tafel constants for anodic and cathodic processes, and electrochemical impedance spectroscopy (EIS). Generally, experimental spectra were then reproduced by an adequate equivalent circuit. From these measurements, the corrosion rate of the WE in contact with electrolyte can be evaluated.

2.2. Experimental setup

Figure 1 presents a descriptive scheme of the experimental setup used in this study. The counter electrode was a stainless-steel grid (Figure 2). The steel rebar, generally used in reinforced concrete, constituted the working electrode (Figure 2) with a drilled hole at one end (Figure 2-b) to ensure electrical connection to the potentiostat. This steel rebar had a smooth surface with a diameter of 10 mm. It was coated with an insulating tape at both ends to limit the contact area with the soil to 5 cm (length). The contact area of the WE for all experiments was then 15.7 cm^2. The reference electrode was a graphite rod (Figure 2) throughout the experimental process. Table 1 shows the potential of the graphite rod embedded in clay with respect to SCE. The potential shows an exponential decay with time. All potentials were related to SCE scale.

First, the CE was placed in the slightly conical mould wall. A small portion of the CE extends above the top surface of the mould, in order to be connected to the potentiostat (Figure 2). Second, the wetted soil, with a water content slightly above the liquid limit W_L, was poured and vibrated. Third, the WE was inserted in the centre of the poured soil. Finally, the RE was inserted between the WE and the CE. The mould was then covered with a pre-cut lid. All

apertures were sealed carefully with silicone mastic to avoid evaporation and to maintain the soil water content throughout the experiment.

The potentiostat used in this study was Gamry® Interface 1000. Once the system was stabilized (i.e. constant OCP), the following procedure was realized:

1. OCP was measured during the first 5 minutes to ascertain the free potential value.

2. EIS was then measured at OCP with a frequency ranging between 100 kHz and 10 mHz or less, by 5 or 10 points per decade. The amplitude of AC signal was 10 mV_{rms}

3. After the collection of impedance spectrum, the electrode was kept at the open circuit for one hour, followed by 5 minutes of OCP measurement.

4. Potentiodynamic polarization curve was then collected. The potential was scanned from -50 to +50 mV with respect to OCP at a scan rate of 1 $mV\ s^{-1}$.

This set of measurements was repeated continuously for 2 days, then once a day for a week, then once a week for one month, then once a month for 3 months and finally every 3 months. Altogether, the experiments were continued for six months.

2.3. Calculation and analyses

From these measurements, two sets of results were obtained, the current I in function of the potential (voltammogram) and the impedance (complex number) in function of the AC perturbing signal. The objective was to evaluate the corrosion current density I_c ($A\ cm^{-2}$) then to calculate the corrosion rate V_c ($\mu m\ y^{-1}$).

From the potentiodynamic voltammetry, I_c was deduced from the first Stern-Geary equation [38] (equation 1) with the faradaic current passing through the WE interface.

$$I_F = I_c \cdot \{exp[b_a \cdot (E - E_c)] - exp[b_c \cdot (E - E_c)]\} \tag{1}$$

In the above equation, "I_F" represents the measured current density ($A\ cm^{-2}$), "I_c" the corrosion current density, "b_a" the Tafel constant of the anodic process (V^{-1}), "b_c" the Tafel constant of the cathodic process (V^{-1}), "E_c" the corrosion potential determined at the zero overall current (V), and "E" is the measured potential (V).

The corrosion rate (Equation 2) was then calculated from the value of corrosion current I_c.

$$V_c = \frac{M \cdot I_c \cdot t}{F \cdot n \cdot \rho} \tag{2}$$

Where "M" ($g\ mol^{-1}$) stands for the molar mass of the steel ($g\ mol^{-1}$) considered to be equal to that of iron, "t" (s) the contact time, "ρ" ($g\ cm^{-3}$) the density of steel rebar, "F" ($A\ s\ mol^{-1}$) the Faraday, and "n" the valence of steel dissolution assimilated to that of iron.

It is important to recall that a typical feature of impedance spectra obtained, involves generally two time constants with capacitive behaviour as illustrated in Figure 3 [16] [27]. This circuit is composed of the electrolyte resistance R_e, the double layer capacitance C_d, the charge transfer resistance R_t, the faradaic capacitance C_F, and the faradaic resistance R_F. The measured current I under potential scan contains therefore, in addition to I_F, the current for the charging of the interface capacitance I_{capa}. The current I measured was then expressed by Equation 3.

$$I = I_F + I_{capa} = I_F + (C_d + C_F).\frac{dE}{dt} \tag{3}$$

Where, dE/dt is the potential scan rate. However, in most cases, I_{capa} was neglected by using sufficiently slow potential scan, thus I_F was considered to be equal to I.

According to the second equation of Stern and Geary (Equation 4) [38], the corrosion current density I_c can be evaluated from the polarization resistance R_p (Ω) and the Tafel constants.

$$I_c = \frac{1}{(b_a - b_c)} \cdot \frac{1}{R_p} \qquad (4)$$

The polarization resistance can be calculated either from the slope of the current-potential curve at the corrosion potential E_c, as well from the impedance results by fitting the impedance spectra with the equivalent electrical circuit or the extrapolation of Nyquist plot to the low frequency limit (Equation 5). Note that R_p does not contain the term of the electrolyte resistance R_e.

$$R_p = R_t + R_F \qquad (5)$$

3. Materials

Three types of soil were analysed in this study: natural silt, kaolinite clay and montmorillonite clay. Their X-ray diffractogram is presented in Figure 4 in order to identify their mineralogy.

The soils were initially moistened to become a mud by adding an appropriate amount of water to the dry natural material.

Table 2 presents the water content of the slurry, w $= (\text{water mass})/(\text{dry soil mass})$, the pH, and the electrical conductivity of the considered soils. The water used was doubly deionised water.

3.1. Natural silt

The natural soil used in this study was silt retrieved from earthmoving works. It constituted the principal component of the earth concrete (cf. Table 3). Based on these properties and its grading curves, the soil used was classified as sandy loam SL(SM) by the USCS classification

(Unified Soil Classification System). According to its XRD (Figure 4), it was mainly composed of quartz (61%), and the clay particles were essentially muscovite, vermiculite, chlorite and illite [8]; these clays are non-swelling in presence of water.

3.2. Kaolinite P300

The kaolinite used was natural clay P300. It is T-O clay (1:1) which corresponds to mineralogy from two layers:

T: Tetrahedral layer composed of a set of silicon (Si) and four anions of oxygen (O^{2-});

O: Octahedral layer composed of a set of two aluminium (Al) and eight hydroxyls (OH^{-}).

This mineralogy type of clays has a low reactivity with its surrounding environment and a low sensitivity to water absorption. Its physical properties are presented in Table 3.

3.3. Montmorillonite

The montmorillonite was also a natural clay of the T-O-T mineralogy (2:1) which is an octahedral layer surrounded by 2 tetrahedral layers. This mineralogy type of clays is highly reactive due to the uncompensated electrical loads on the edge of the sheet. Thus, this type of clay is reactive with its environment, and swells with the presence of water. Its properties are summarized in Table 3.

4. Results

The interaction of three different clays in contact with a smooth steel rebar was analysed using two complementary methods: potentiodynamic voltammetry around the OCP and the electrochemical impedance spectroscopy EIS.

4.1. Potentiodynamic voltammetry results

Figure 5 displays the time evolution of log(I)-E curves for steel-Montmorillonite couple. One over two experimental data were plotted by symbols. Lines corresponds to fitted curves according to Equation 2 by non-linear simplex regression calculation. The consistency between these two data was satisfactory since the coefficient of determination R^2, the correction factor, was greater than 0.999 for all cases.

Excluding the very early stage, it can be noticed that the cathodic current density increased with contact time of the steel in the soil whereas the anodic reaction rate decreased. The potential shifted towards a more anodic direction while the corrosion current density I_c decreased. Following, the variation of various voltammetry parameters for the three soils was presented.

4.1.1. OCP and E_c variation

Figure 6 presents the variation of the measured E_{oc} (OCP) and E_c that was calculated by non-linear fitting of I-E curves (Equation 2). The curves were slightly consistent. Both potentials varied similarly. In the case of silt, it increased in the first three days, while in the case of kaolinite, it increased in the first ten days. Both then decreased. In contrast, for montmorillonite, they decreased monotonically in the first 2 days and then increased after.

4.1.2. Variation of corrosion current density

Figure 7 shows the variation of the corrosion current density I_c determined by potentiodynamic voltammetry, Equation 2. Like the potential variation, I_c of silt and kaolinite presented a similar feature. The initial I_c was low, 0.7 and 1.3 $\mu A \ cm^{-2}$, respectively for silt and kaolinite. It decreased slightly on the first day of contact time; then it remained almost constant for about a week, then increased steeply after. This steep current increase was

somewhat unexpected and will be compared to I_c calculated from the impedance data (§4.2.4). On the contrary, for the montmorillonite, the I_c started with a high value of 2.2 $\mu A\ cm^{-2}$, then decreased monotonically until it reached, after 100 days of contact time, a constant curve at about 0.4 $\mu A\ cm^{-2}$.

4.1.3. Variation of Tafel constants

Figure 8 illustrates the variation of Tafel constants b_a and b_c. As for the anodic constants, they did not vary significantly compared to the cathodic ones. For silt and kaolinite, b_a change depicted a sigmoid. At early contact time, it was about 40 V^{-1} and changed slightly during the first four days, then it decreased for one month, till it reached the steady state value, 16 V^{-1}. In the case of montmorillonite, b_a was initially equal to that of silt, then increased from 39 to 60 V^{-1}, then decreased to reach a constant curve of 24 V^{-1}.

The amplitude of b_c changed often as mentioned above. As for steel-silt interface, b_c was initially about -42 V^{-1}, then decreased on the first 5 days. It reached -120 V^{-1}. After 5 days, b_c increased and approached -23 V^{-1}. For kaolinite, which was the case for anodic Tafel constant, a similar shape was depicted but its values shifted towards more negative values (-71 to -130 V^{-1} and about to -51 V^{-1} after four months). In the case of montmorillonite, b_c change has showed a sigmoid, -28 to -80 V^{-1}. The half plateau value was located around three days.

4.2. EIS results

Figure 9 presents the impedance spectra of steel-clay interface collected at an early stage of the experiments. For other systems, a similar impedance diagram was observed. They revealed two depressed capacitive loops in Nyquist diagram. Therefore, the equivalent circuit

will be composed of the electrolyte resistance R_e, two resistances (charge transfer resistance R_t and faradaic resistance R_F), and their corresponding capacitances. This circuit was very close to Figure 3, where the capacitive behaviour was presented by pure capacitance; whereas in Figure 10-a, reckon depressed feature of capacitive loops, CPE was used. The CPE_{Cd} represented the contribution of the electrochemical double layer capacitance. The couple $R_F//CPE_F$ was allocated to the redox process taking place with corrosion products and accumulated on the steel surface. The electrochemical reaction involving a redox process is presented in §5.2. On the contrary, for montmorillonite, after about 20 days of contact with the steel rebar, an additional capacitive loop started to appear in the Nyquist diagram at the high frequency side and increased after about 2 months. The equivalent circuit presented in Figure 10 was used for parameter fitting calculations.

The circuit elements in Figure 10 are the following:

R_e: Electrolyte resistance between RE and WE ($\Omega\ cm^2$)

R_t: Charge transfer resistance ($\Omega\ cm^2$)

Q_{Cd}:   CPE element for double layer capacitance ($F\ cm^{-2}\ s^{1-a_{Cd}}$)

a_{Cd}:   Power coefficient of CPE (dimensionless)

R_F: Faradaic resistance associated with redox process ($\Omega\ cm^2$)

Q_F: CPE element for faradaic capacitance ($F\ cm^{-2}\ s^{1-a_F}$)

a_F: Power coefficient of CPE for the redox process (dimensionless)

R_{SL}:   Resistance representing ionic conduction through the surface layer ($\Omega\ cm^2$)

Q_{SL}:   CPE element for surface layer ($F\ cm^{-2}\ s^{1-a_{SL}}$)

a_{SL}:   Power coefficient of surface layer (dimensionless)

The impedance of a CPE element (Q, a) in parallel with a resistance R is:

$$Z = \frac{1}{\frac{1}{R} + Q \cdot (J \cdot \omega)^a}$$ (6)

The results of fitting calculation were superimposed on experimental data in Figure 9. They represented well the experimental data. The variation of the different circuit's parameters is described below.

4.2.1. Variation of the electrolyte resistance R_e

Figure 11 presents the variation of electrolyte resistance R_e of steel rebar in contact with three different soils. R_e for silt and kaolinite soils was about 10 times greater than that of montmorillonite. R_e was almost constant about 3.0 and 2.3 $k\Omega \, cm^2$ for silt and kaolinite respectively, but it increased slightly after 3 months of contact and reached 4.9 and 3.1 $k\Omega \, cm^2$ respectively for silt and kaolinite.

As for montmorillonite, R_e decreased from 0.26 to 0.21 $k\Omega \, cm^2$ during the first 17 days then increased to 0.54 $k\Omega \, cm^2$ after 6 months of the experiment.

4.2.2. Variation of the two resistances R_t and R_F.

Figure 12 exhibits the variation of the charge transfer resistance R_t and the faradaic resistance R_F. For montmorillonite, excluding at the early stage, R_t (solid symbol with bold curve) was smaller than R_F (open symbol with thin curve). Besides, R_t data were scattered substantially, and the time variation was unpredictable. R_t for silt was initially ca. 7 $k\Omega \, cm^2$, then decreased down to 2.5 $k\Omega \, cm^2$, then increased almost linearly to 30 $k\Omega \, cm^2$ after eight months of contact with the soil. R_F increased almost-linearly from 10 to 25 $k\Omega \, cm^2$ during the first 2 days, then it remained constant.

R_t for kaolinite showed a bell-shaped curve. The initial and final values were both 2.8 $k\Omega$ cm^2 and the resistance was maximal at 3 days with 11 $k\Omega$ cm^2. R_F increased similarly for silt, but slightly steeper, almost-linearly from 6 to 40 $k\Omega$ cm^2 for 30 days to reach a steady state. R_t for montmorillonite was almost constant around 3 $k\Omega$ cm^2, on the first day, then decreased to 1 $k\Omega$ cm^2 at about four days. Over one week, it increased almost linearly. Its R_F was smaller than R_t in contrast to other cases. It depicted sigmoid, from 2 to 25 $k\Omega$ cm^2.

4.2.3. *Variation of the effective capacities C_{Cd} and C_F*

The quantitative comparison of CPE was not an easy task since this variable was defined in both CPE element Q and power coefficient a. For that reason, the effective capacitance of each CPE element was calculated using the equation proposed by Brug et al. [39]. For a circuit R_e-(CPE//R_t), i.e. composed of electrolyte resistance R_e in series with a parallel linking of CPE element and the charge transfer resistance R_t, the effective capacitance C can be expressed by equation 7:

$$C = Q^{\frac{1}{a}} \cdot \left(\frac{1}{R_e} + \frac{1}{R_t} \right)^{\frac{a-1}{a}}$$

(7)

Figure 13 presents the variation of the effective double layer capacitance C_{Cd} and the faradic capacitance C_F.

C_{Cd} (solid symbols with bold curve) for both silt and kaolinite increased with contact time. For silt, it changed from 50 μF cm^{-2} during one hour of contact time to 10 mF cm^{-2} after 9 months. For kaolinite, it ranged between 60 μF cm^{-2} and 16 mF cm^{-2} for the same period. Between one and two weeks, the capacitance increase was slower and was about 700 μF cm^{-2}.

For montmorillonite, its variation was different. It increased from 80 to 700 $\mu F\ cm^{-2}$ during the first month and then decreased significantly.

C_F of silt was small at the beginning, 35 $\mu F\ cm^{-2}$ and reached a value as high as 25 $mF\ cm^{-2}$ after 6 months of contact time. C_F for kaolinite remained constant during the first day, then it increased progressively. After 8 months, it was about 6 $mF\ cm^{-2}$. The variation of this capacitance for montmorillonite was complex; it increased slightly during the first day, then it decreased from 400 to 70 $\mu F\ cm^{-2}$ for 2 days, then it increased after. The value at 8 months was the smallest among the three soils examined.

4.2.4. *Variation of the corrosion current density*

Using Equation 3, the corrosion current density I_c was evaluated from EIS data. So, called Stern-Geary constant B was determined by parameters fitting of voltammogram, Figure 8. Figure 14 displays the variation of the corrosion current density I_c calculated with R_p as mentioned above (Equation 6). This relationship was introduced to an electrochemical system with anodic and cathodic Tafel relationship. However, the same equation was valid when a redox process was involved in the corrosion mechanism [40]. Figure 7 shows the same relationship when I_c was determined from polarization curves. The initial I_c values were similar for these two methods. However, a marked divergence can be noticed for a long contact time. I_c determined by EIS decreased continuously up to three months, then I_c increased very slightly for silt and kaolinite; whereas for montmorillonite, I_c decreased during the whole period examined in this study.

Figure 7 includes also the corrosion rate expressed by thickness loss. After 8 months, the corrosion rate was smaller than 3 $\mu m\ y^{-1}$ for all clayey soils examined.

5. Discussion

5.1. Identification of corrosion products

The corrosion products formed at the surface of steel rebar were studied by XPS and XRD. XPS analysis was carried out between 0 and 1350 eV after etching during 720 s of the electrode surface. Figure 15 presents, as for an example, the XPS spectrum of corrosion products in contact with montmorillonite, after two years exposure, around the peak corresponding to Fe2p. The results of deconvolution of this peak were indicated in the figure. The Fe^{2+} peak corresponds to Fe_2O_3. The peak Fe^{3+} corresponded to the magnetite formed by a transformation of $Fe(OH)_2$. The multiple peaks indicated the presence of magnetite. A small amount of siderite, $FeCO_3$ was also detected.

The XRD also detected, not illustrated here, the magnetite and the peaks of montmorillonite, quartz and goethite (α-FeOOH). For the other two corrosive environments, XPS spectra were similar and identified the same substances with slightly different proportion for peak area. XRD pattern showed the presence of magnetite.

The main corrosion product was therefore magnetite. According to E-pH diagram, in neutral medium, which is our case at the beginning of experiments (cf. Table 2), OCP for the three media examined (located between -0.54 and -0.75 V vs. SCE) indicated that Fe_3O_4 was thermodynamically stable species [41]. The examined corrosion products formed on the steel rebar embedded in clayey soils were mainly magnetite with a small amount of siderite. According to Nakono, with geochemistry database [42], $Fe(OH)^+$ will be formed in this potential - pH domain.

5.2. Corrosion process

In most cases, the impedance spectra showed two capacitive loops. These two capacitive loop diagrams can be explained by the following corrosion mechanism:

- For the anodic process:

$$Fe + OH^- \rightarrow Fe(OH)_{ads} + e^- \tag{1}$$

$$Fe(OH)_{ads} \rightarrow Fe(OH)^+_{aq} + e^- \tag{2}$$

$$Fe(OH)_{ads} + OH^- \rightarrow Fe(OH)_2 + e^- \tag{3}$$

$$Fe(OH)_2 + 2Fe + 6OH^- \Leftrightarrow Fe_3O_4 + 4H_2O + 6e^- \tag{4}$$

$$Fe_3O_4 + 4H_2O \rightarrow 3Fe^{3+} + 8OH^- + e^- \tag{5}$$
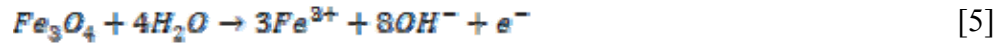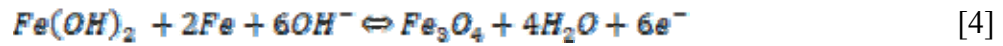
Reaction of Step [1] is the formation of monovalent adsorbed species. This intermediate reaction species leads to the active dissolution through reaction [2] and the formation of passive species $Fe(OH)_2$ by reaction [3]. The latter is oxidized into Fe_3O_4 (reaction [4]). These species dissolve further in ferric species by reaction [5]. Step [4] is reversible giving rise to the faradaic capacitance C_F. Two intermediate reactions, $Fe(OH)_{ads}$ and $Fe(OH)_2$ at the surface, may induce two relaxation time constants. However, no such time constants were observed. This phenomenon can be explained by the fact that these time constants were too short to be observed experimentally.

- The cathodic process will be the reduction of dissolved oxygen:

$$O_2 + 2H_2O + 4e^- \rightarrow 4OH^- \tag{6}$$

All these reactions were electrochemical with charge transfer. Step [4] was reversible, which induced a capacitive behaviour in electrochemical impedance. Corrosion process was governed by the equality of the electron formation (Steps 1 to 5) and their consumption (Step

6). Results suggested that a large amount of Fe_3O_4 will be formed because C_F value was high (cf. Figure 13).

To facilitate the discussion, the surface film formed will be called magnetite even if siderite was also detected.

In the three soils media, the cathodic Tafel constant b_c was never close to zero (cf. Figure 8) excluding that of the reaction kinetics (Step 6) because it was never entirely controlled by the diffusion, in spite of the electrode embedded in a pasty soil. The diffusion limiting current density of dissolved oxygen should be lower in the presence of clays than that for an electrode directly immersed in a solution; the voltammetry curves did not show that the cathodic process was controlled by convective diffusion. Thus, Step 6 was mostly governed by the activation process.

On the other hand, the anodic branch did not show that I_F was independent of the potential; whereas the dissolution of passive species may be chemical. According to Seo and Sato [43], the anion-doped hydro-oxide may depend on the potential of the electrode.

OCP corresponded to the overall current density equal to 0 ($I = I_a + I_c = 0$). If magnetite film become more stable with time, the reaction rate of Step 5 may decrease, leading OCP moving towards a more anodic direction (Figure 5).

5.3. Loop appearance at high frequencies for Montmorillonite

The insert in Figure 16 illustrates the additional high frequency loop observed for this clay after 6 months of contact time. This loop can be simulated with a CPE//R. The calculated R_t remained practically constant and it was equal to 200 $\Omega\ cm^2$ with respect to contact time. The resistance associated with the high frequency loop was about 200 $\Omega\ cm^2$. The effective capacitance was equal to 0.04 $\mu F\ cm^{-2}$. This high frequency loop was likely due to the

formation of a compact montmorillonite layer, probably containing corrosion products, on the steel rebar surface. By applying a flat condenser model with the following equation, the thickness of this layer will be estimated:

$$C = \frac{\varepsilon_0 \cdot \varepsilon_r \cdot A}{d}$$ (8)

Where "ε_0" is the vacuum permittivity ($8.85 \ 10^{-14} \ F \ cm^{-2}$), "$\varepsilon_r$" the relative permittivity of the corrosion product, "A" the contact surface area (here 1 cm^2) and "d" the film thickness (cm). According to the results of Zakri [44], ε_r of montmorillonite is equal to 33. Therefore, the compact surface layer thickness was estimated as 0.7 μm.

5.4. Corrosion current density I_c

When analysing I_c, estimated from voltammetry curves (Figure 7), it can be noted that the minimum value was quite similar in the case of the three soils, even though it was twice as much for kaolinite. On the other hand, we noticed also an increase in I_c value after 4 days for the silt and one month for the kaolinite. This behaviour was not detected for the montmorillonite for 6 months.

At the beginning of the tests, I_c can be classified as follows: montmorillonite >> kaolinite > silt. This classification corresponded to the quantity of water added during the preparation of the sample. The initial water content appeared to play an important role in the corrosion kinetics of the steel rebar during the first days. Once the corrosion was accelerated beyond one month, the classification of I_c was reversed silt > kaolinite >> montmorillonite.

5.5. Effective capacitance

Corrosion can induce an increase in the actual area of the electrode by increasing the surface roughness. To check if the current variation was related to electrode area or corrosion kinetics, we should compare the double layer capacitance C_d.

Figure 13 shows that C_d change was similar in both value and evolution over time, up to 30 hours of steel-soil contact. They increased almost linearly in the semi-logarithmic plane, i.e. their increase followed an exponential law. Some acceleration of their increase was observed when I_c increased rapidly (excluding the case of montmorillonite). For the last clay sample, we observed a formation of a relatively thin protective film. The continuous decrease of I_c as well as C_d in the latter medium can be explained by the formation of the barrier layer.

The faradaic capacitance C_F (open symbols with thin curves) in Figure 13, gave information on the redox process of Step 4. The greater the amount of magnetite available for the reversible reaction was, the larger the C_F value was. During one day of contact, C_F remained stable. The steel-silt system was initially about five times smaller but later it increased to reach the value like the other two media. Hence, at the beginning, there will be less amount of the magnetite in this environment that have low water content. Steps 1 and 3 in this environment would be slower. However, C_F increased after this initial period and continued to increase thereafter.

For kaolinite, the C_F value remained stable for one day, and then it increased. However, I_c also increased after the first day. Therefore, a strong correlation existed between C_F and I_c for the steel electrode in contact with kaolinite. As for silt, the C_F value indicated a continuous increase in surface accumulation of magnetite and an increase of I_c determined by voltammetry after 10 hours of contact. C_F variation for the steel-montmorillonite interface was more complex.

It can be noticed that C_d and C_F varied similarly (excluding the case of montmorillonite above one day of contact time). A particular behaviour of montmorillonite can be explained by the formation of a compact surface layer. The magnetite is an electronic conducting species, therefore, the increase of C_F, that was the amount of magnetite at the steel surface cause a

greater C_d value. In other terms, C_d was not merely related to the surface roughness of the steel, but also to the expanded surface area of corrosion products accumulated on the steel surface. At the very beginning of experiments, where the accumulation of magnetite on the steel surface was negligible, the value of C_d that was frequently observed for the double layer capacitance, was several tens of $\mu F \ cm^{-2}$.

5.6. Charge transfer resistance R_t and Faradaic resistance R_F

Excluding the early stage of the steel corrosion in contact with montmorillonite, t < 3 days, the lower the corrosion current density determined by the voltammetry was, the greater the charge transfer resistance was (Figure 12). This was rather an unusual situation. However, C_F (Figure 13) and R_t varied qualitatively in a similar way. The charge transfer resistance also involved the reaction step [4], and during that period, magnetite formed had lost its reactivity. The formation of a surface film with montmorillonite may likely be related to this phenomenon.

It can be seen that R_F (Figure 12) was strongly correlated with I_c, the higher R_F was, the higher the corrosion current density was. An exception occurred for a short contact period for montmorillonite where we found out that $R_t < R_F$. Thus, the corrosion current density was expected to decrease with contact time. However, we realized that the increase in R_F was fast between one and ten days for montmorillonite. Precisely, in this period, C_F decreased. Since C_F was related to the charge stored at the interface, the decrease in the reactivity of the passive film lead to a lower quantity of this species available for the redox reaction of Step 4.

The corrosion rate depended on both the anodic and cathodic processes. The corrosion potential was defined by the equality of these two current densities in absolute value. Variation of OCP, measured just before the start of the voltammetry measurement, is discussed below.

5.7. OCP and E_c

Figure 6 shows that at early contact time, OCP remained almost constant for silt, whereas it increased for kaolinite and decreased for montmorillonite. After one day of contact, OCP shifted towards a more anodic direction for all the three interfaces. For silt and kaolinite, OCP showed a maximum than decreased; whereas for montmorillonite, it continued to increase. The higher the I_c was, the more anodic OCP was.

Figure 17 presents the potential variation at anodic or cathodic current equal to ± 2 μA cm^{-2} for the three systems examined. These potentials varied similarly to OCP, i.e. the decrease of the corrosion current I_c determined by voltammetry was induced by the slow-down of both processes. Conversely, the increase of corrosion current density was determined by the acceleration of both processes.

We realized a difference between OCP and E_c for the three steel-clay interfaces. E_c was determined by the overall zero current on the voltammetry plots (Figure 6). The gap was small at the beginning of the experiment and then increased with time. However, the steel-silt and steel-kaolinite systems showed a larger difference compared with montmorillonite medium.

The origin of this potential difference between OCP and E_c is discussed in the next section.

5.8. Effect of interface capacitance to I_c

As shown in Equation 3, the current measured during voltammetry experiments contained the current for charging the interface capacitance whereas the corrosion rate should be determined by the faradaic current I_F. Consequently, the current measured by voltammetry curve overestimated the corrosion current density. Figure 13 shows that the interface capacitance, C

($= C_d + C_F$) increased from ca. 200 µF cm^{-2} to more than 10 mF cm^{-2} for silt and kaolinite media.

For C = 1 mF cm^{-2} with the scan rate dE/dt = 1 mV s^{-1}, I_{capa} = 1 µA cm^{-2}. When C reached this magnitude, we observed a significant increase of I_c by voltammetry for silt and kaolinite media. As for montmorillonite, after 10 days, C decreased, and Figure 7 shows the corrosion current density decreasing with time.

In Figure 18, the voltammograms corrected for the charging current of interface capacitance is presented for steel-silt at two months contact time. Figure 18-a is relative to the linear I-E curve. The correction for charging current decreased the current while increasing the polarization resistance. It increased from 5.06 to 12.9 kΩ cm^{-2} by subtracting the contribution of the interface capacitance. E_c, i.e. the zero overall current, shifted towards a more anodic direction by 21 mV. E_c was determined by the correction of interface capacitance and was equal to OCP. It was thus demonstrated that the difference of OCP and E_c observed was really induced by the potential scan, certainly too fast for these corroding systems because of a marked increase of interface capacitance.

Figure 18-b displays the same results in the Tafel plot. The fitting of these curves with Equation 2 resulted in an I_c equal to 2.39 and 0.856 µA cm^{-2}.

The corrosion kinetics by impedance measurement required the Stern-Geary coefficient B [38]. B determined by parameter fitting calculation of the measured current density and that of the corrected C charging, cf. Figure 18-a, was respectively 12.1 and 11.0 mV. The former was probably slightly higher because the effect of ohmic drop by R_e. These two values, however, were sufficiently close enough to the accuracy of corrosion current density expected for the corrosion study. Consequently, the B value obtained without the correction of C can be

used to evaluate the corrosion current density by R_p determined from the impedance measurements. R_p determined by EIS did not contain the electrolyte resistance R_e.

5.9. Corrosion rate of steel embedded in different clays

Figure 14 shows the corrosion current density determined from the polarization resistance which was calculated from EIS data used in equation 4. The corrosion was fast at the beginning of experiments, and then decreased with contact time. At the beginning, steel-montmorillonite interface exhibited the fastest corrosion rate, that was more than 3 $\mu A\ cm^{-2}$ after two hours of contact.

It is important to remark that the presence of electrolyte resistance underestimated the corrosion rate by voltammetry method. Figure 9 shows that the electrolyte resistance was not negligible compared with the polarization resistance for silt and kaolinite media in a short contact time. The comparison of Figures 7 and 14 confirmed that the corrosion current density determined by voltammetry was lower than that of the EIS method. On the other hand, the interface capacitance C $(=C_d+C_F)$ overestimated the corrosion current density by voltammetry method. Figure 13 shows that the interface capacitance C increased with contact time leading to the overestimation of the corrosion current density. It resulted in antagonistic effects. Only the EIS allowed evaluating these two parameters.

For the case of steel-silt couple, it was revealed that the smallest corrosion current density occurred at the beginning, was almost four times smaller than the steel embedded in montmorillonite. However, after four months of contact time, all systems lead to the same I_c, ca. 0.3 $\mu A\ cm^{-2}$. In terms of the corrosion rate, the current density corresponded to the thickness loss of 3 $\mu m\ y^{-1}$ for the dissolution of iron into ferrous species. Note that if the corrosion process was taking place with ferric species, as proposed in Reaction step [5], the corrosion rate will be 2 $\mu m\ y^{-1}$.

Clayey soils examined in this work did not have a significant influence on the corrosion rate of a steel rebar in contact with a clayey soil. Montmorillonite can act as a protection by developing a barrier layer at the surface of the bar. The corrosion rate obtained supported the use of steel rebars in raw earth construction.

6. Conclusion

In this paper, we investigated the interaction between three types of clayey soil and steel rebars by means of electrochemical methods. The objective of the study was to estimate the corrosion kinetics to check the feasibility of the reinforcement of earth concrete. The two electrochemical methods used were potentiodynamic voltammetry and EIS.

Results showed that a passive film, constituted mainly of magnetite was formed in large quantity. For the corrosion mechanism proposed, the corrosion rate was better correlated to the polarization resistance than to the charge transfer one. The water content played a determining role both in the kinetics and in the quality of the passive coating. Corrosion may induce an increase in the actual area of the electrode by increasing its surface roughness. It can also induce a faradaic capacitance associated with a redox process involving the passive species. Overall, the anodic dissolution of the steel and the cathodic reduction of dissolved oxygen in clayey soil decreased with the time of contact with clays.

It was shown that EIS measurements supplied a reliable value of the corrosion current density. A similar variation was observed for kaolinite and silt 6 hours after the beginning of experiments and valued at about 15 μm y^{-1}. The steel-montmorillonite couple presented the highest corrosion rate at the beginning. For the three couples examined, the corrosion rate decreased to about 3 μm y^{-1}. It can be concluded that the type of clay has no significant influence on the corrosion rate of a steel bar. This observation enhanced the importance of experiments carried out for a longer period.

The corrosion rate evaluated after 6 months of contact time was acceptable for the lifetime of the structure. According to this study, it was possible to use steel rebar in reinforced raw earth concrete.

In perspective, the carbonation and the ingress of chloride ions in earth concrete will be investigated for a longer exposure of raw earth building.

Acknowledgements

7. References

[1] W. H. Langer and B. F. Arbogast, "Environmental Impacts Of Mining Natural Aggregate," in *Deposit and Geoenvironmental Models for Resource Exploitation and Environmental Security*, vol. 80, G. G. M. R. (. Fabbri A.G., Ed., Dordrecht, Springer Netherlands, 2002, pp. 151-169.

[2] M. D. Gavriletea, "Environmental Impacts of Sand Exploitation. Analysis of Sand Market," *Sustainability,* vol. 9, no. 7, 2017.

[3] J. Morel, A. Mesbah, M. Oggero and P. Walker, "Building Houses with local materials: means to drastically reduce the environmental impact of construction," *Building and Environment,* vol. 36, pp. 1119-1126, 2001.

[4] F. F. Pacheco-Torgal and S. Jalali, "Earth construction: Lessons from the past for future eco-efficient construction," *Construction and Building Materials,* vol. 29, pp. 512-519, 2012.

[5] P. Melià, G. Ruggieri, S. Sabbadini and G. Dotelli, "Environmental impacts of natural and conventional building materials: a case study on earth plasters," *Cleaner Production,* vol. 80, pp. 179-186, 2014.

[6] J. Eid, "New construction material based on raw earth: cracking mechanisms, corrosion phenomena and physico-chemical interactions," *European Journal of Environmental and Civil*

Engineering, 2017.

[7] A. Hibouche, "Sols traités aux liants. Performances hydro-mécaniques et hygrothermiques. Applications en BTP," Ph.D. Thesis, Université Le Havre Normandie, Le Havre, 2013.

[8] J. Eid, "Elaboration d'un éco-géo-matériau à base de terre crue.," Ph.D. Thesis, Université Le Havre Normandie, Le Havre, 2016.

[9] J. M. Kanema, J. Eid and S. Taibi, "Shrinkage of earth concrete amended with recycled aggregates and superplasticizer. Impact on mechanical properties and cracks.," *Materials and Design,* vol. 109, pp. 378-389, 5 November 2016.

[10] J. Eid, S. Taibi, J. M. Fleureau and M. Hattab, "Drying, cracks and shrinkage evolution of a natural silt intended for a new earth building material. Impact of reinforcement," *Construction and Building Materials,* vol. 86, pp. 120-132, 2015.

[11] A. Harison, A. Agrawal and A. Imam, "Bamboo as an Alternative to Steel for Green Construction Towards Low Cost Housing," *Journal of Environmental Nanotechnology,* vol. 6, no. 2, pp. 100-104, 2017.

[12] A. Javadian, M. Wielopolski, I. F. Smith and D. E. Hebel, "Bond-behavior study of newly developed bamboo-composite reinforcement in concrete," *Construction and Building Materials,* vol. 122, pp. 110-117, 2016.

[13] D. Ribeiro and J. Abrantes, "Application of electrochemical impedance spectroscopy (EIS) to monitor the corrosion of reinforced concrete: A new approach," *Construction and Building Materials,* vol. 111, pp. 98-104, 2016.

[14] M. Stefanoni, U. Angst and B. Elsener, "Corrosion rate of carbon steel in carbonated concrete – A critical review," *Cement and Concrete Research,* Vols. In Press, Corrected Proof, 2017.

[15] C. G. Berrocal, K. Lundgren and I. Löfgren, "Corrosion of steel bars embedded in fibre reinforced concrete under chloride attack: State of the art," *Cement and Concrete Research,* vol. 80, pp. 69-85, 2016.

[16] V. d. F. C. Lins, M. L. M. Ferreira and P. A. Saliba, "Corrosion Resistance of API X52 Carbon Steel in Soil Environment," *Journal of Materials Research and Technology,* vol. 1, no. 3, pp. 161-166, 2012.

[17] B. He, P. Hanb, C. Lu and X. Bai, "Effect of soil particle size on the corrosion behavior of natural gas pipeline," *Engineering Failure Analysis,* vol. 58, pp. 19-30, 2015.

[18] B. He, P. Han, L. Hou, D. Zhang and X. Bai, "Understanding the effect of soil particle size on corrosion behavior of natural gas pipeline via modelling and corrosion micromorphology," *Engineering Failure Analysis,* vol. 80, pp. 325-340, 2017.

[19] M. Yan, C. Sun, J. Dong, J. Xu and W. Ke, "Electrochemical investigation on steel corrosion in iron-rich clay," *Corrosion Science,* vol. 97, pp. 62-73, 2015.

[20] A. El-Shamy, M. Shehata and A. Ismail, "Effect ofmoisture contents of bentonitic clay on the corrosion behavior of steel pipelines," *Applied Clay Science,* vol. 114, pp. 461-466, 2015.

[21] R. Akkouche, C. Rémazeilles, M. Jeannin, M. Barbalat, R. Sabot and P. Refait, "Influence of soil moisture on the corrosion processes of carbon steel in artificial soil: Active area and differential aeration cells," *Electrochimica Acta,* vol. 213, pp. 698-708, 2016.

[22] V. P. Perez and A. Alfantazi, "Effects of Oxygen and Sulfate Concentrations on the Corrosion Behavior of Zinc in NaCl Solutions," *CORROSION,* vol. 68, no. 3, pp. 1-11, 2012.

[23] C. Soriano and A. Alfantazi, "Corrosion behavior of galvanized steel due to typical soil organics," *Construction and Building Materials,* vol. 102, pp. 904-912, 2016.

[24] S. Kaufhold, A. W. Hassel, D. Sanders and R. Dohrmann, "Corrosion of high-level radioactive waste iron-canisters in contact with bentonite," *Journal of Hazardous Materials,* vol. 285, pp. 464-473, 2015.

[25] T. Ishidera, K. Ueno, S. Kurosawa and T. Suyama, "Investigation of montmorillonite alteration and form of iron corrosion products in compacted bentonite in contact with carbon steel for ten years," *Physics and Chemistry of the Earth,* vol. 33, pp. 269-275, 2008.

[26] M. L. Schlegel, C. Bataillon, F. Brucker, C. Blanc, D. Prêt, E. Foy and M. Chorro, "Corrosion of metal iron in contact with anoxic clay at 90°C: Characterization of the corrosion products after two years of interaction," *Applied Geochemistry,* vol. 51, pp. 1-14, 2014.

[27] M. Yan, C. Sun, J. Xu, J. Dong and W. Ke, "Role of Fe oxides in corrosion of pipeline steel in a red clay soil," *Corrosion Science,* vol. 80, pp. 309-317, 2014.

[28] C. Rémazeilles, D. Neff, J. Bourdoiseau, R. Sabot, M. Jeannin and P. Refait, "Role of previously formed corrosion product layers on sulfide-assisted corrosion of iron archaeological artefacts in soil," *Corrosion Science,* vol. 129, pp. 169-178, 2017.

[29] D. Neff, *Apport des analogues archéologiques à l'estimation des vitesses moyennes et à l'étude des mécanismes de corrosion à très long terme des aciers non alliés dans les sols.,* Compiègne: Thèse, Université de Technologie de Compiègne, 2003.

[30] I. Cole and D. Marney, "The science of pipe corrosion: A review of the literature on the corrosion of ferrous metals in soils," *Corrosion Science,* vol. 56, pp. 5-16, 2012.

[31] Y. El Mendili, A. Abdelouas, A. Ait Chaou, J.-F. Bardeau and M. Schlegel, "Carbon steel corrosion in clay-rich environment," *Corrosion Science,* vol. 88, pp. 56-65, 2014.

[32] M. Snapp, S. Tucker-Kulesza and W. Koehn, "Electrical resisitivity of mechancially stablized earth

wall backfill," *Journal of Applied Geophysics,* vol. 141, pp. 98-106, 2017.

[33] R. Browne, "The performance of concrete structures in the marine environment," in *Symposium on Corrosion in the marine environment, International Corrosion Conference, Institute of Marine Engineers*, London, 1973.

[34] Y. Liu and R. Weyers, Modeling the time to corrosion cracking of the cover concrete in chloride contaminated reinforced concrete structures, Blacksburg Virginia: PhD Dissertation, 1996.

[35] A. Nasser, "La corrosion des aciers dans le béton à l'état passif et par carbonatation: Prise en compte des courants galvaniques et des défauts d'interface acier-béton," Toulouse, 2010.

[36] E. Vega, "Altération des objets ferreux archéologiques du site de Glinet (Seine-maritime, France, XVIe siècle) Caractérisation des produits de corrosion et étude des mécanismes," Belfort-Montbeliard, 2004.

[37] J. Baron and J. P. Ollivier, Les bétons, bases et données pour leur formulation, Paris: Eyrolles, 1996.

[38] A. Stern and J. Geary, "Electrochemical Polarization: A Theoretical Analysis of the Shape of Polarization Curves," *Journal of Electrochemical Society,* vol. 104, pp. 56-63, 1957.

[39] G. Brug, A. v. d. Eeden, M. Sluyters-Rehbach and J. Sluyters, "The analysis of electrode impedances complicated by the presence of a constant phase element," *Journal of Electroanalytical Chemistry and Interfacial Electrochemistry,* vol. 176, no. 1-2, pp. 275-295, 1984.

[40] I. Epelboin, C. Gabrielli, M. Keddam and H. Takenouti, "Alternating-Current Impedance Measurements Applied to Corrosion Studies and Corrosion-Rate Determination," *Electrochemical Corrosion Testing,* pp. 150-192, 1981.

[41] M. Pourbaix, Atlas of electrochemical equilibria in aqueous solutions, 2 ed., Houston: National Association of Corrosion Engineers, 1974.

[42] N. Takeno, "Atlas of Eh-pH diagrams," Geological Survey of Japan, Tokyo, 2005.

[43] M. Seo and N. Sato, "Dissolution of Hydrous Metal Oxides in Acid Solutions," *Boshoku Gijutsu,* vol. 24, pp. 399-402, 1975.

[44] T. Zakri, "Contribution à l'étude des propriétés diélectriques de matériaux poreux en vue de l'estimation de leur teneur en eau : modèles de mélange et résultats expérimentaux," Grenoble, 1997.

Figures
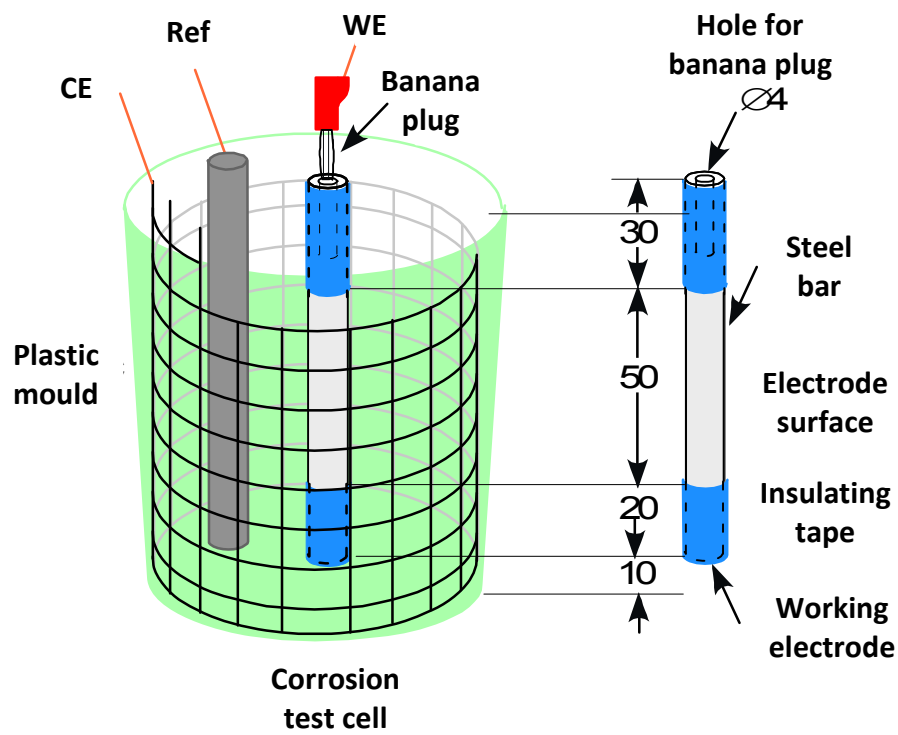
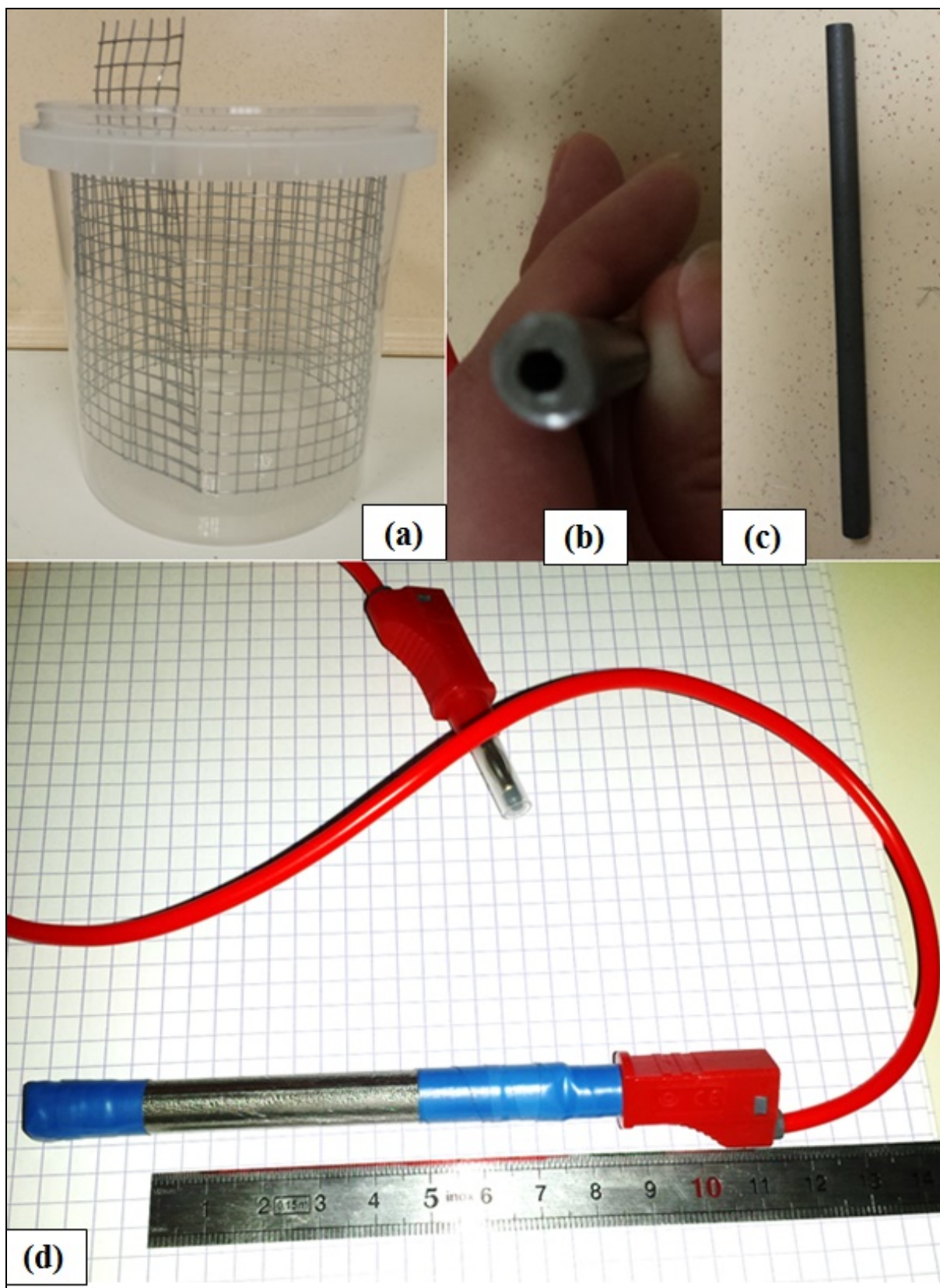**Figure 1- Electrochemical cell with soil as electrolyte.**

Figure 2- Electrodes: a-stainless steel grid as CE; b-hole of the WE; c-graphite bar as RE; d-WE.
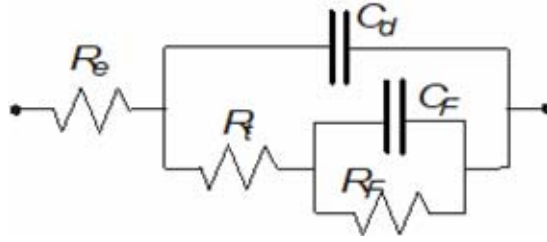
Figure 3- Typical Equivalent electrical circuit for clay-steel interface.
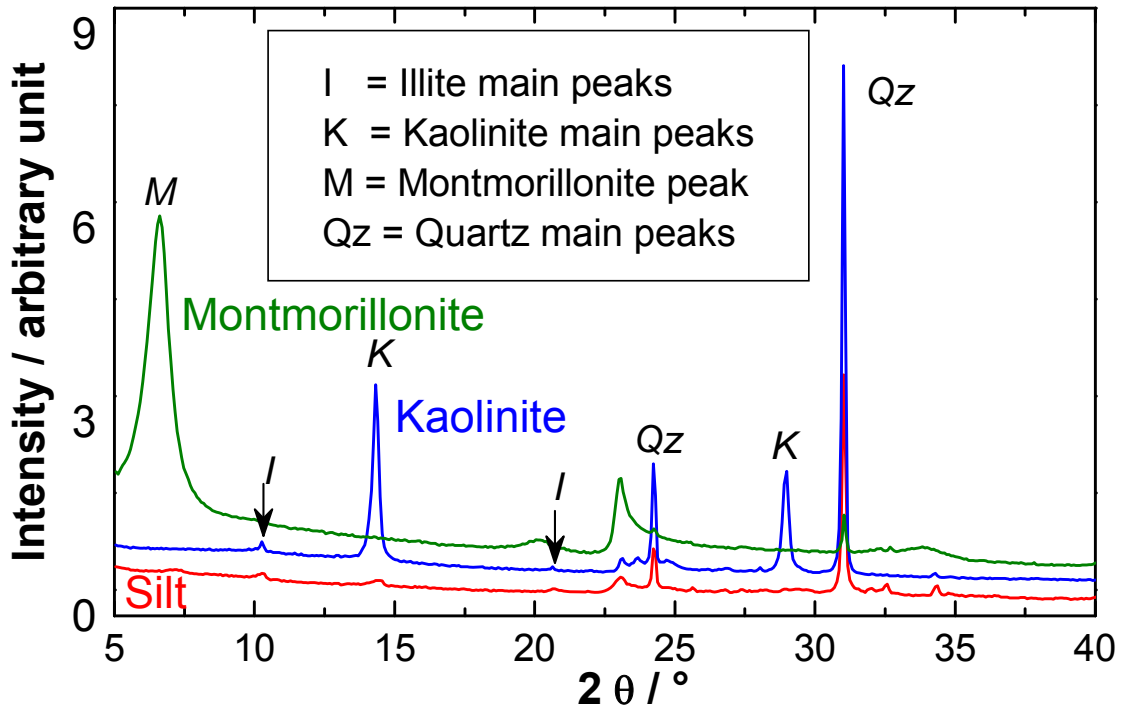

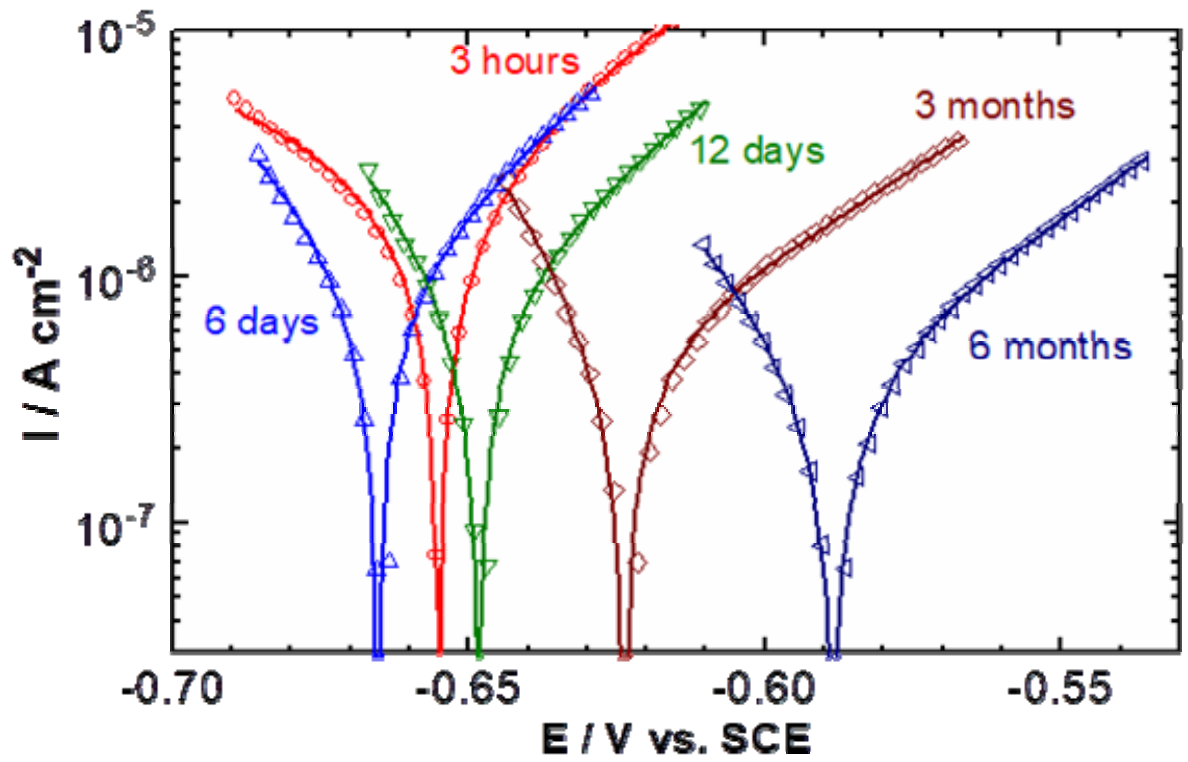**Figure 4- X-ray diffractogram of the three soils used. RX source is Cobalt (Co)**

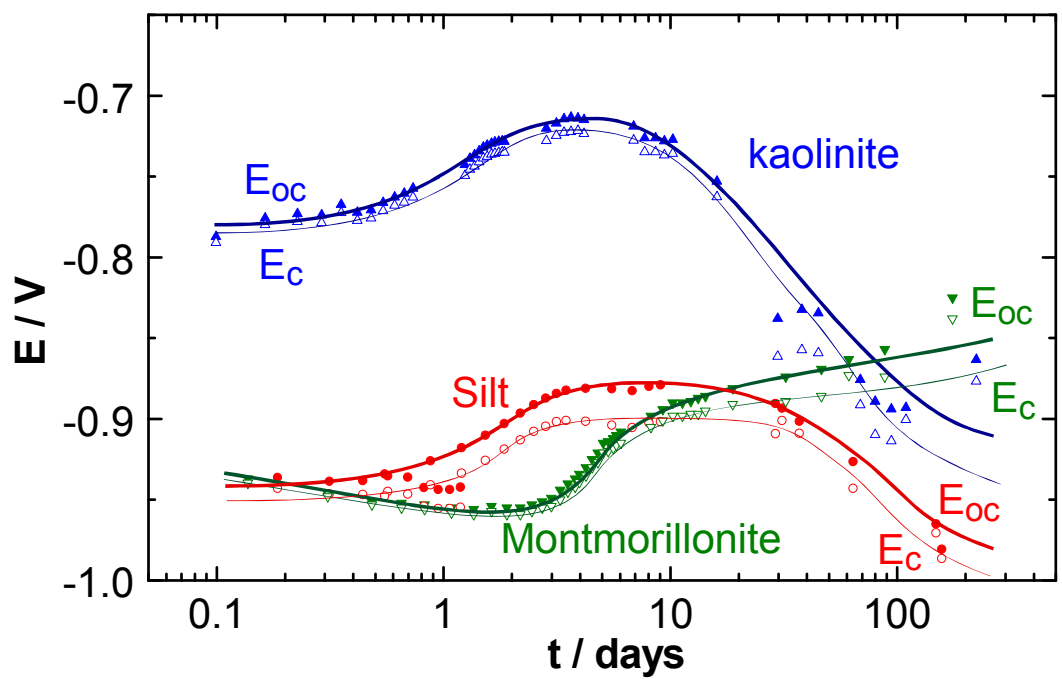**Figure 5- Voltammograms of Steel/Montmorillonite at different contact times.**

Figure 6- E$_{oc}$ and E$_c$ change with respect to contact time of three different soils.
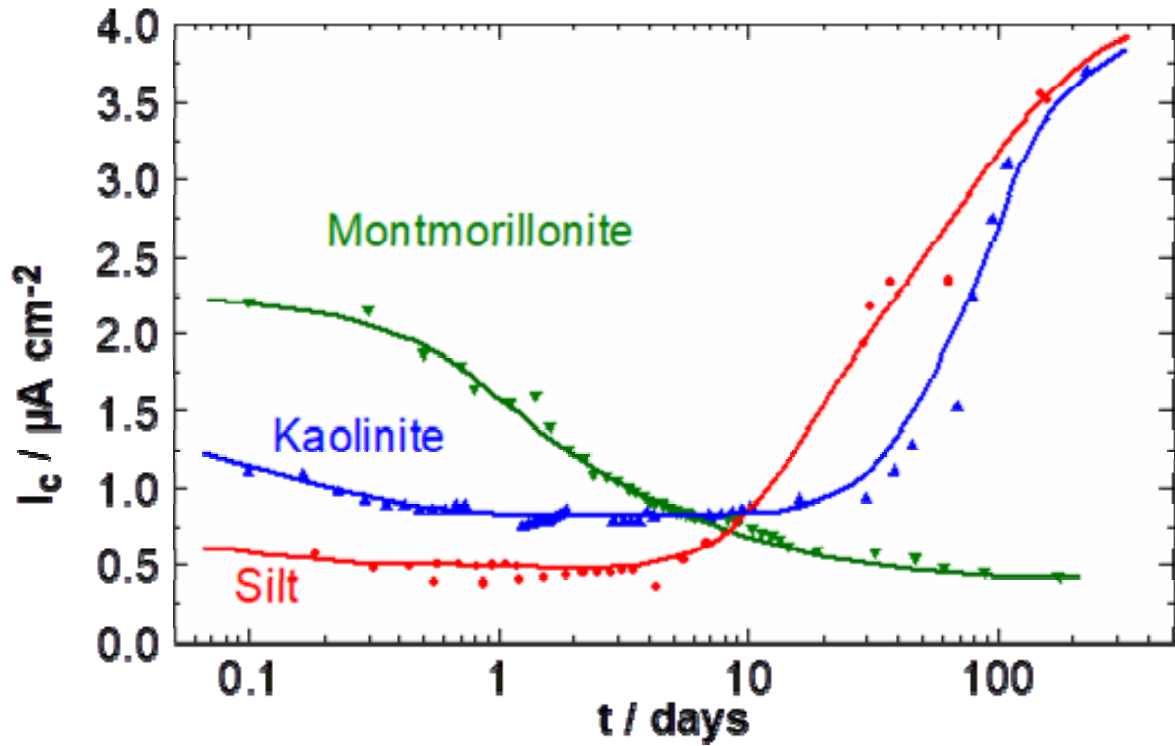
Figure 7- Variation of corrosion current density I_c evaluated by voltammetry with respect to contact time for three soils examined.
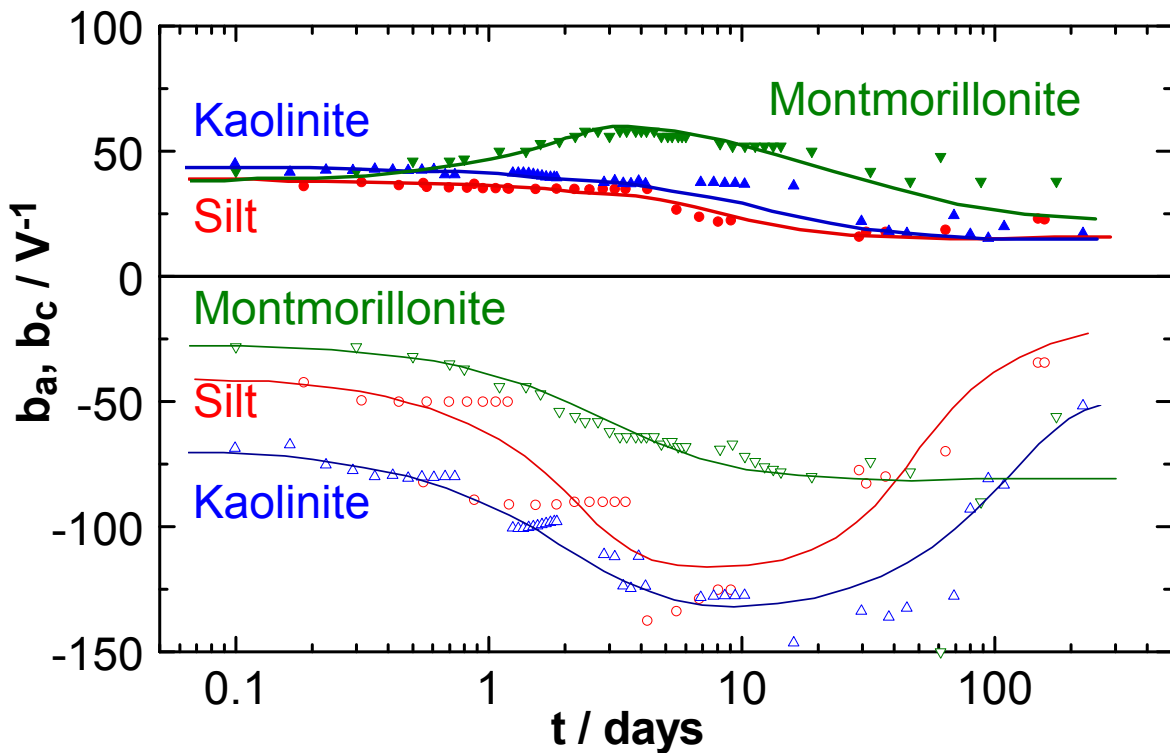
Figure 8- Variation of Tafel constant, b_a and b_c with respect to contact time for three soils examine.
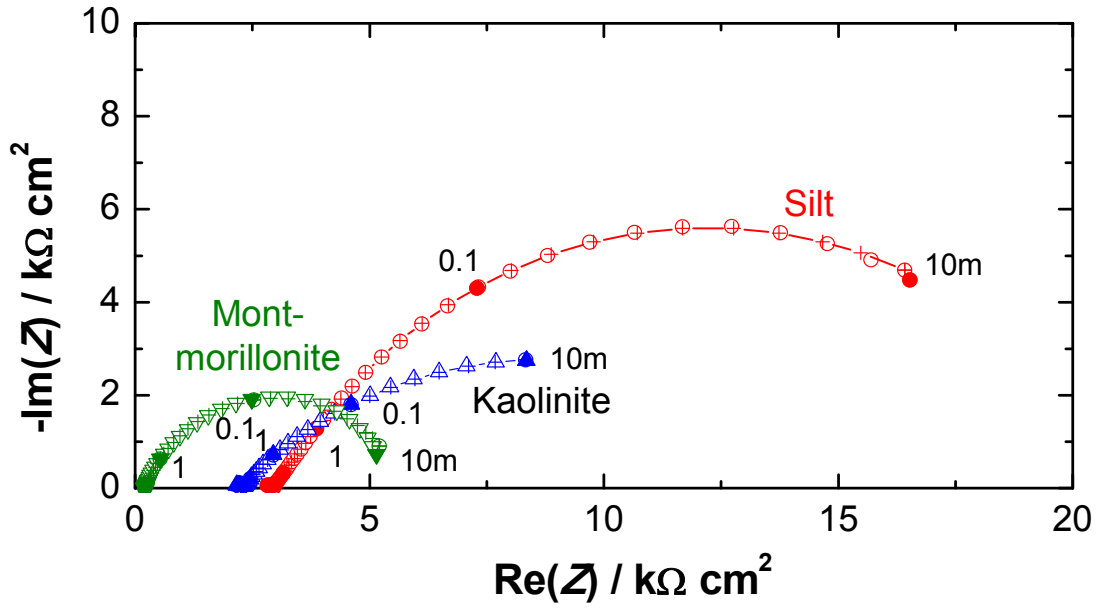
Figure 9- Impedance spectra in Nyquist plot of steel bar embedded in three soils studied at six hours contact time" —□—" for fitted data. Parameters are frequency in Hz.
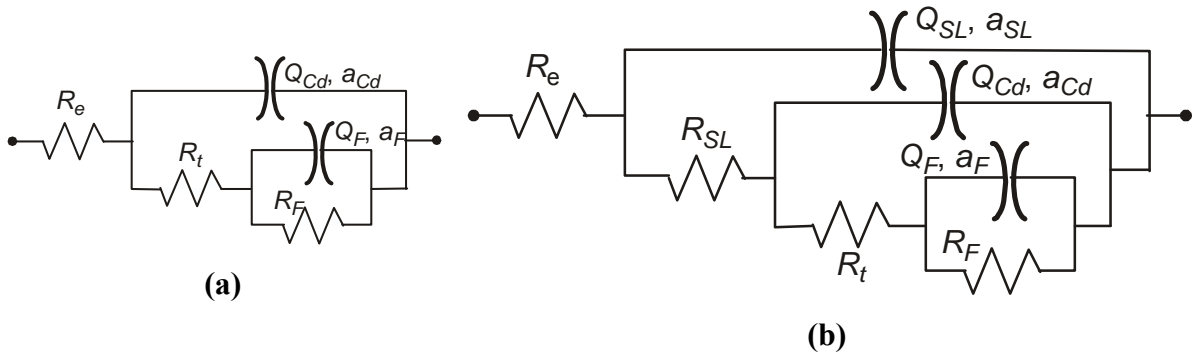
Figure 10- Electrical equivalent circuit to reproduce experimental data (a) two capacitive loops (b) three capacitive loops observed for steel / montmorillonite interface for a long contact time.
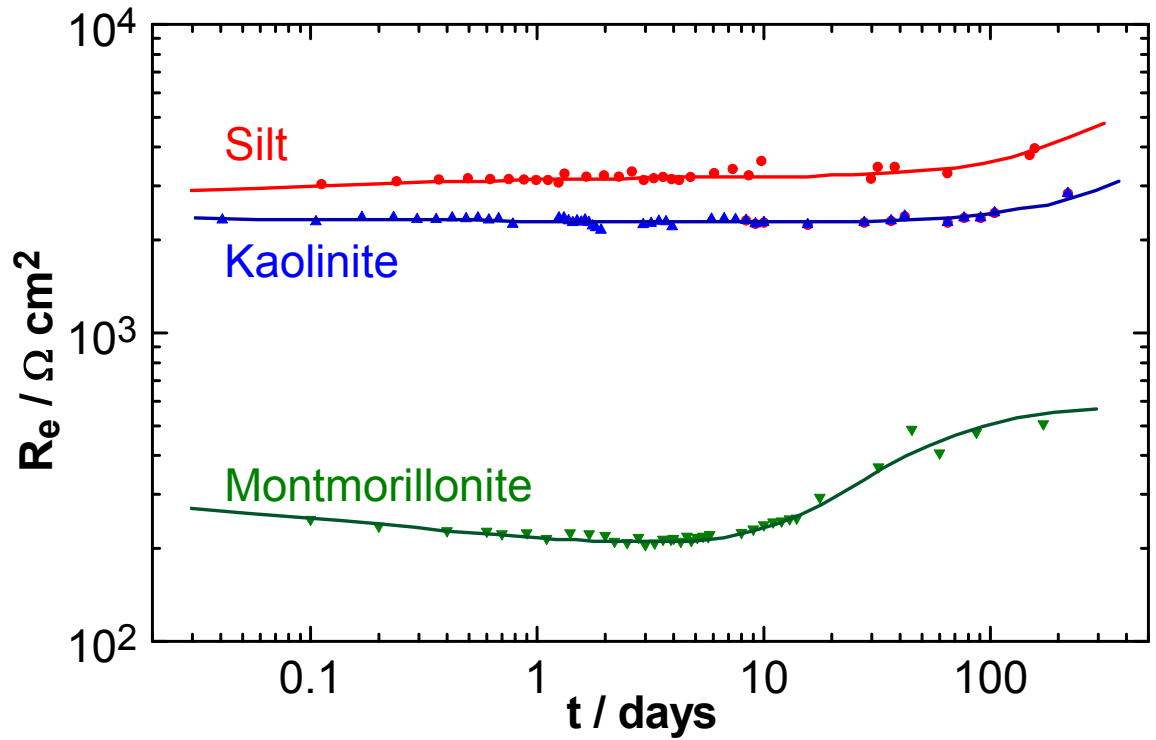
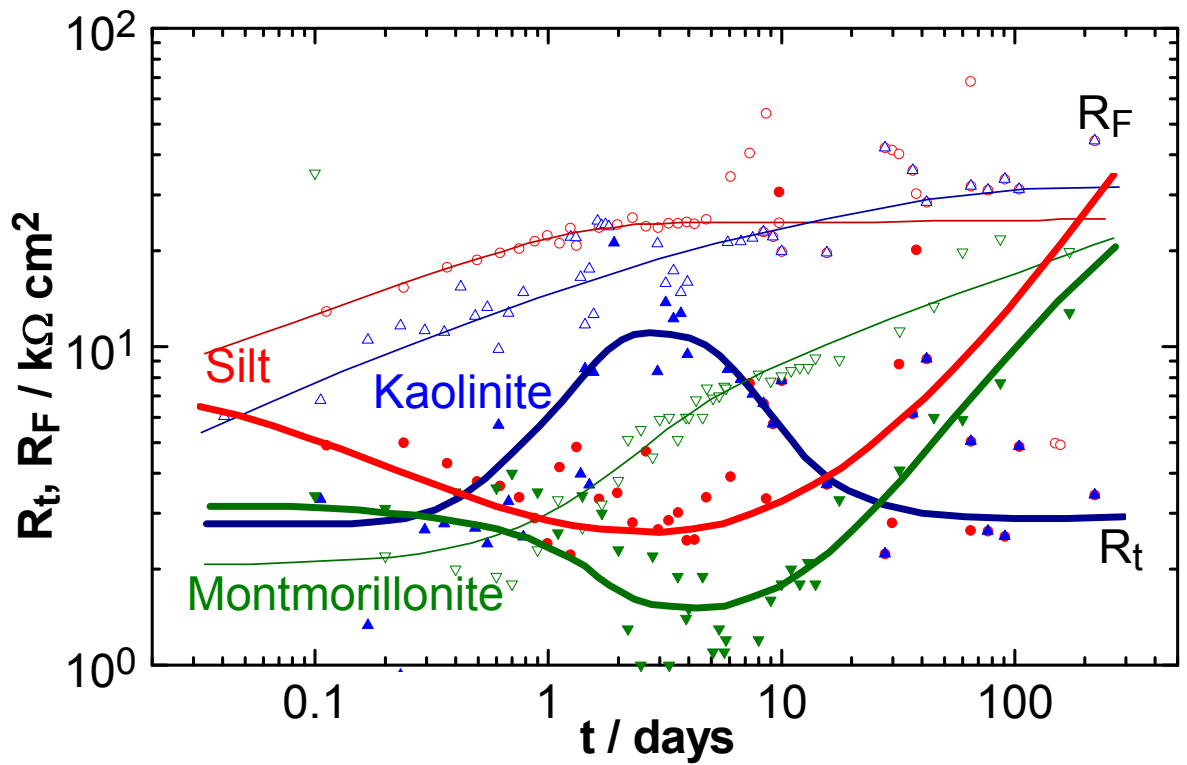**Figure 11- Time change of the electrolyte resistance for steel electrode in contact with three different soils**

Figure 12- Time change of R_t and R_F for steel in contact with different soils. Solid symbols and bold curves for R_t and open symbol and thin curves for R_F
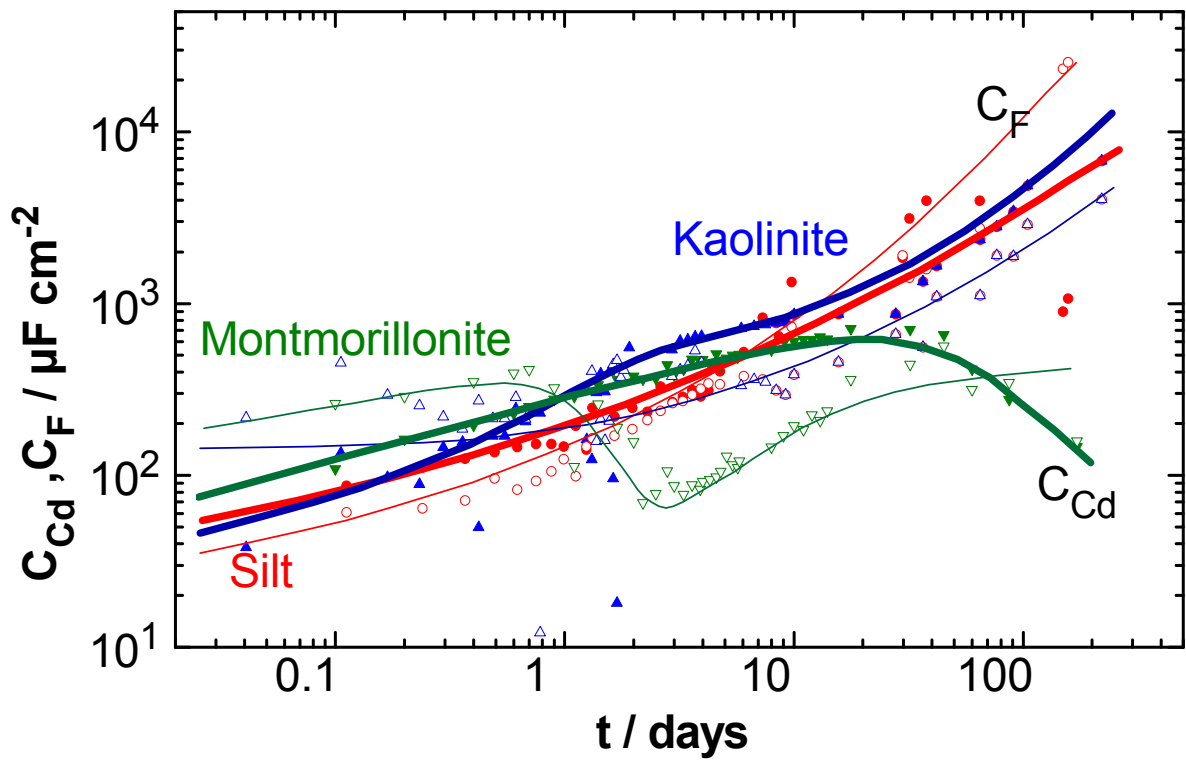
Figure 13- Effective capacitance C_{Cd} (solid symbols with thick curve) and C_F (open symbols with fine curves) for steel / soil interface with respect to contact time
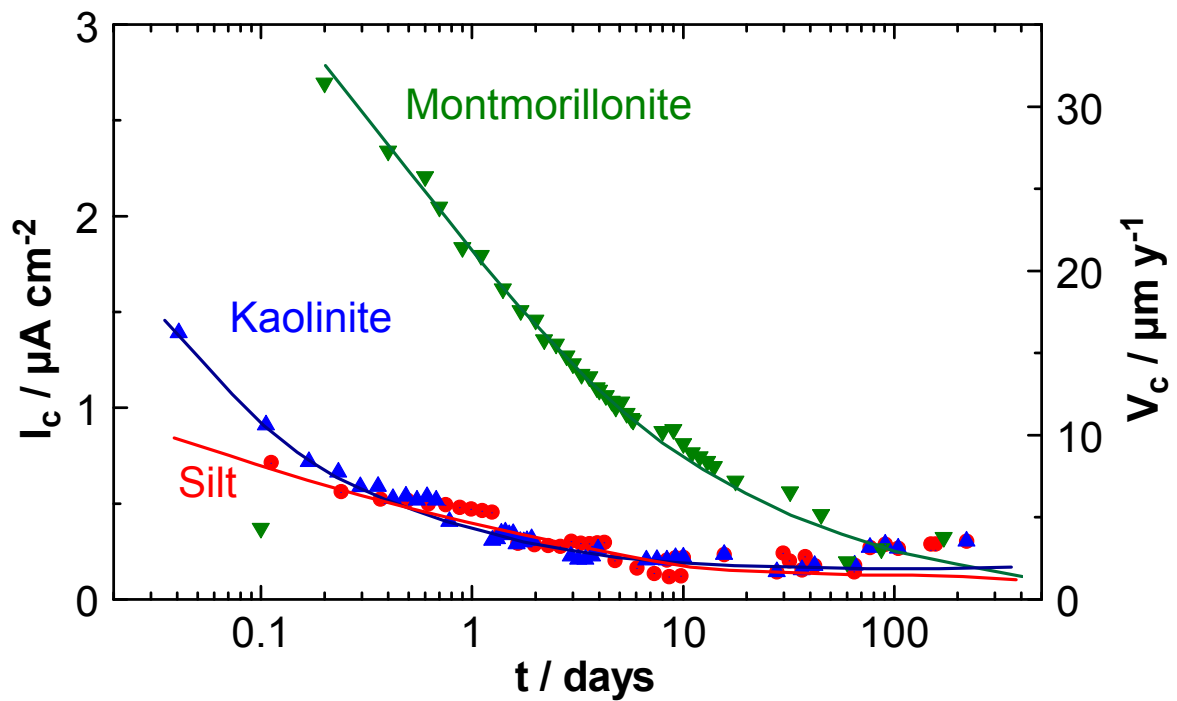

Figure 14- Corrosion current density determined by EIS measurements with respect to contact time for three soils.
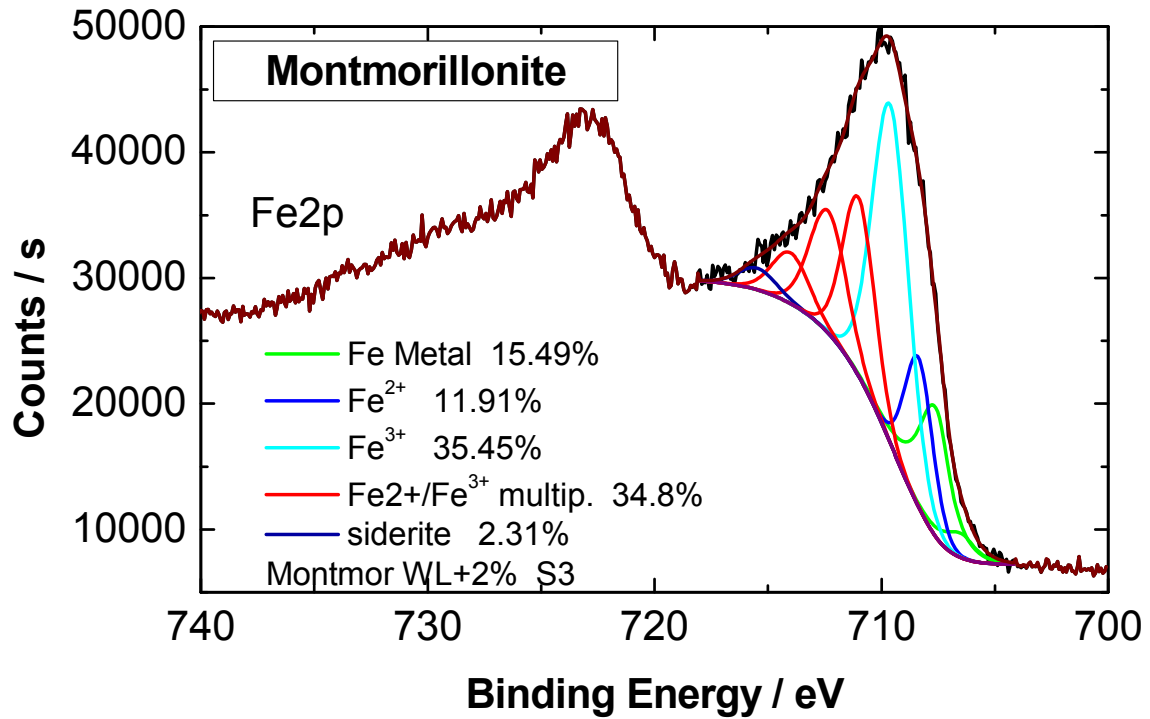
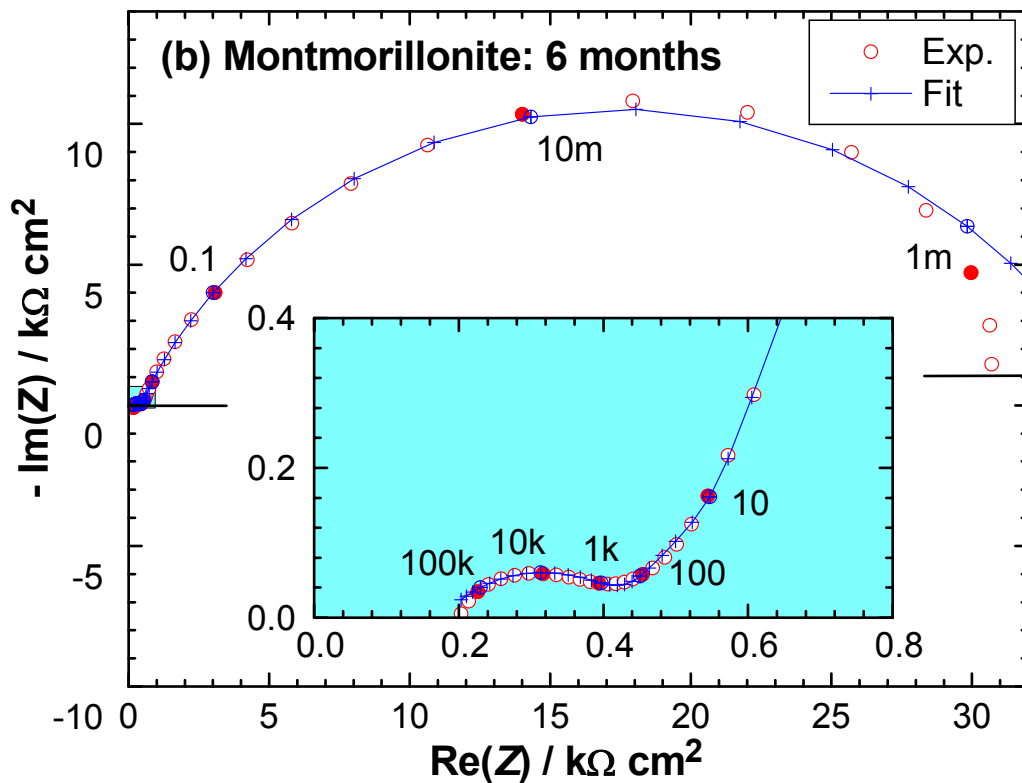**Figure 15- XPS spectra of steel bar embedded into montmorillonite for two years**

Figure 16- Appearance of High frequency loop for montmorillonite after 6 months of contact time.
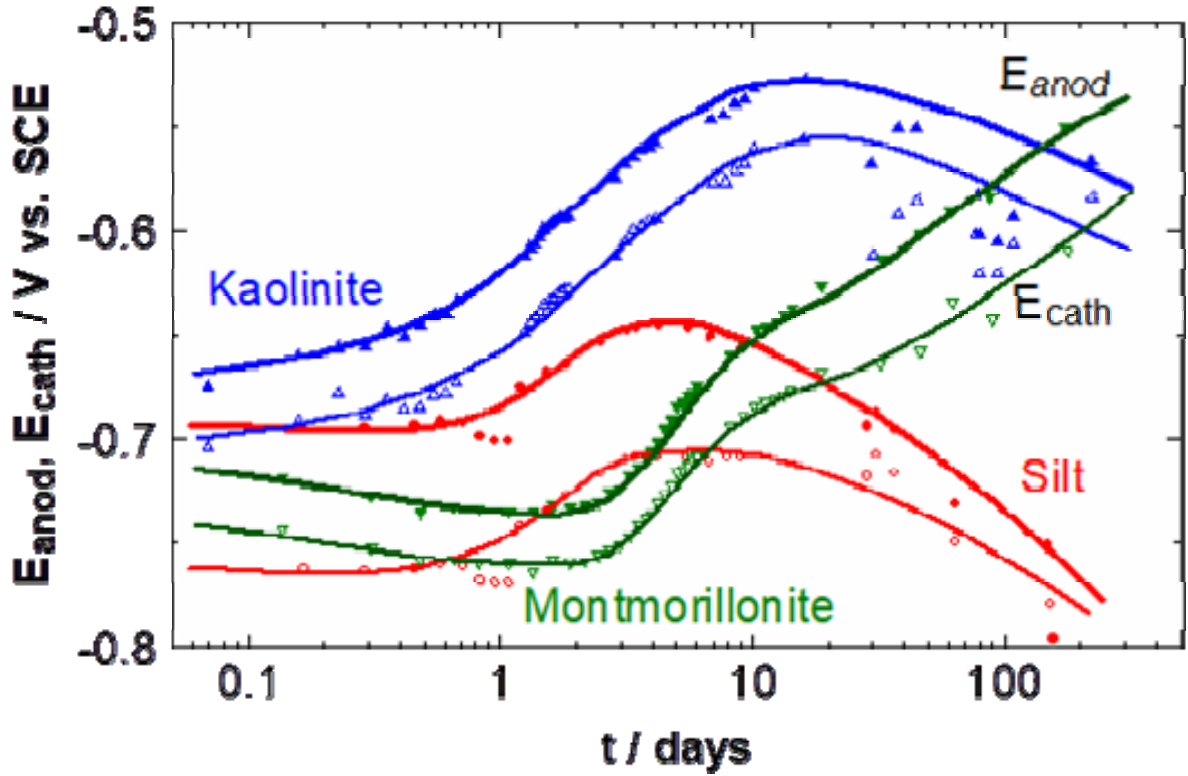
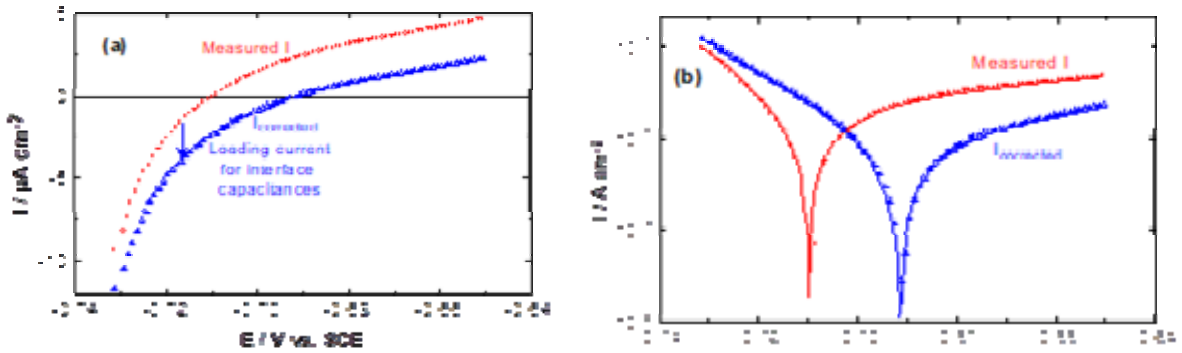**Figure 17- Time evolution of potential at I = 2 or 2 µA cm^{-2} for steel / soil interface.**

Figure 18- Effect of capacitance loading current on I (V) curve. Steel / silt interface at two months of contact time. C$_{Cd}$=2.33 mF cm^{-2} and C$_F$=1.13 mF cm^{-2}

Tables

Table 1- Potential of graphite electrode with respect to SCE for three mud

$E_{graphite} = E_\infty + \Delta E \cdot \exp(-t/tau)$

Mud	E_∞/ V vs. SCE	ΔE / V	tau / day
Natural silt	0.20	0.014	7.40
Kaolinite	0.30	-0.20	19.7
Montmorillonite	0.25	0.042	13.3

Table 2- Initial state of the mud

	Natural Silt	Kaolinite	Montmorillonite
pH	8.0 ± 0.2	7.92 ± 0.2	7.51 ± 0.13
Conductivity (µS/cm)	47.6 ± 2	46.61 ± 2	172 ± 2
Water content (%)	26	52	125

Table 3- Soils properties

	Natural Silt	Kaolinite	Montmorillonite
Methylene Bleu Value: VBS	0.5	--	--
Liquid Limit: W_L (%)[1]	20	40	116
Plasticity Index: IP	6	19	70
Fines content (<80 µm) (%)	35	100	100
Clay (<2µm) (%)	0	60	69
Silt (2µm to 60 µm) (%)	25	40	--
Sand (0.06 mm to 2 mm) (%)	67	0	--
Gravel (>2mm) (%)	8	0	--
D_{10} (µm)	32	0.1	--
$C_u = D_{60}/D_{10}$	4.37	20	--
$Cc = \dfrac{D_{10}^2}{D_{60} \cdot D_{10}}$	0.94	0.45	--

[1] W_L = Liquid Limit of Soil. It is the water content limit before the soil becomes liquid, i.e. no shear strength.

Table 4- Results of parameter fitting of data presented in Figure 15

	As measured	Corrected for capacitance loading current
E_c (V)	0.710 ± 0	-0.691 ± 0
I_c (µA cm^{-2})	2.39 ± 0.04	0.856 ± 0.027
b_a (V^{-1})	11.3 ± 0.333	25.3 ± 1.05
b_c (V^{-1})	-71.5 ± 0.9	-65.9 ± 0.7
R^2	0.9983	0.9998